

Synthesis and Optical Properties of Different Bismuth Niobate Films Grown by Dual Magnetron Co-Sputtering

Osmary Depablos-Rivera,* Andreas Zeinert, and Sandra E. Rodil

The interest about the synthesis of bismuth niobates (BNOs) in a thin-film form has recently grown since their optical and electrical properties are attractive for applications such as photocatalysis, sensors, and fuel cells. The aim of this work is to demonstrate the successful synthesis of different BNOs as films using dual confocal magnetron co-sputtering deposition, and evaluate properly their optical properties. Two independent targets of α - Bi_2O_3 and Nb are used. Crystalline as-deposited films are obtained at Nb contents ≤ 9.2 at%. Meanwhile, films grow amorphous for Nb contents > 9.2 at%. However, amorphous films are crystallized after annealing obtaining BNOs in compliance with the as-grown composition. There is a good reproducibility and correlation between the films structure and composition that is controlled through the variation of the power applied to the Nb target. The following niobates are obtained: solid solutions with 5.1–6.6 at% Nb and $\text{II-Bi}_3\text{NbO}_7$, $\text{Bi}_5\text{Nb}_3\text{O}_{15}$, and the mixture of α - BiNbO_4 (76 wt%) + β - BiNbO_4 (24 wt%). The optical properties of the BNOs are estimated from the data measured by UV-Visible-NIR transmittance and reflectance spectrometry. It is shown that all the films have refractive indexes $n > 2$ and optical gaps between 1.67 and 3.34 eV, depending on the Nb content and phase.

processes,^[1] and some of them have other interesting functional properties such as ferroelectric and magnetic properties.^[2] In addition, the BO-based semiconductors have low toxicity,^[3] chemical stability,^[4] and it has been shown that different micro or nanostructures can be obtained.^[5] The ternary bismuth niobium oxides, also known as bismuth niobates (BNOs), have been reported as good ionic conductors,^[6] photocatalysts,^[7] and high- k dielectric constant materials.^[8]

The BNOs belong to the pseudo-binary system Bi_2O_3 – Nb_2O_5 . The first work about this system was done by Roth and Waring,^[9] who proposed a phase diagram where many BNOs phases were observed. Sample preparation was done mixing the binary oxides at different proportions, finding different phases and compounds through X-ray diffraction (XRD) measurements. Later on, most of these BNOs phases^[9] were reproduced and classified according to their structure by Zhou et al.^[10] as type I–IV. For that work, the authors^[10] mixed Bi_2O_3 and Nb_2O_5 powders using Nb_2O_5 molar percentages between 4.68 and 50%, equivalent to 1.84 and 16.67 atomic (at) % of Nb, respectively.

Type I is a bcc structure, and the type-I BNOs are solid solutions with Nb content between 1.84 and 3.85 at%, equivalent to Nb/Bi atomic ratios from 0.05 to 0.11. Type II is based on the defective fluorite-type structure of the δ - Bi_2O_3 , which has 25% of anionic vacancies; this type of structure is presented in solid solutions with Nb concentrations between 3.85 and 9.09 at%, (Nb/Bi ratio between 0.11 and 0.33). The type II solid solutions have been described as periodically incommensurable superlattices in the three crystalline directions.^[10] Type III structure is tetragonal with a $3 \times 3 \times 7$ fluorite-type supercell; the niobates with this structure have 9.09–11.35 at% of Nb content (Nb/Bi ratio between 0.33 and 0.47). One example of type III is the Bi_3NbO_7 compound with 9.09 at% of Nb^[10]; however, other researchers^[6d,11] reported that the type III- Bi_3NbO_7 is obtained at high temperatures (800–900 °C), while a type II- Bi_3NbO_7 structure is obtained below 800 °C. Finally, Zhou et al.^[10] described the type IV structure as tetragonal with Nb content between 11.35 and 13.04 at% (Nb/Bi ratio: 0.47–0.60), and they considered $\text{Bi}_5\text{Nb}_3\text{O}_{15}$ as the representative compound of this structure. Nevertheless, it is also categorized as a mixed-layer Aurivillius-phase composed by two parts: $[(\text{Bi}_2\text{O}_2)^{2+} (\text{NbO}_4)^{3-}]^- [(\text{Bi}_2\text{O}_2)^{2+} (\text{BiNb}_2\text{O}_7)^-]^+$ with an orthorhombic lattice.^[12]


1. Introduction

Ternary oxides based on bismuth oxide (BO) such as bismuth vanadates, tungstates, molybdates, titanates, and perovskite-type bismuth ferrites have attracted attention because they have shown good performance as catalysts in photo-induced

Dr. O. Depablos-Rivera
Instituto de Ciencias Aplicadas y Tecnología
UNAM
Circuito Exterior s/n, Cd. Universitaria, Ciudad de México, C.P. 045 10, Mexico
E-mail: osmary.depablos@ccadet.unam.mx; osmarydep@yahoo.com

Prof. Dr. A. Zeinert
Laboratoire de Physique de la Matière Condensée
Université de Picardie Jules Verne
33 rue Saint Leu, 80039 Amiens Cedex 1, France

Dr. O. Depablos-Rivera, Prof. Dr. S.E. Rodil
Instituto de Investigaciones en Materiales
UNAM
Circuito Exterior s/n, Cd. Universitaria, Ciudad de México, C.P. 045 10, Mexico

 The ORCID identification number(s) for the author(s) of this article can be found under <https://doi.org/10.1002/adem.201800269>.

DOI: 10.1002/adem.201800269

Another BNO compound frequently reported is BiNbO_4 that is not within the classification proposed by Zhou et al.^[10] BiNbO_4 has 16.67 at% Nb ($\text{Nb}/\text{Bi} = 1$) and is orthorhombic ($\alpha\text{-BiNbO}_4$) at temperatures below 1020 °C and triclinic ($\beta\text{-BiNbO}_4$) above 1020 °C up to its melting point (1240 °C). More recently, Chezhina et al.^[13] have produced BNOs phases by solid state reaction in order to evaluate the magnetic susceptibility and the effect of doping with *d*-elements in the structure, electrical and magnetic properties.

However, as mentioned above, the properties of BNOs are more attractive if the material can be synthesized as thin films. The miniaturization of high-tech electronic devices, such as electronic micro-circuits for communication tools, micro solid oxide fuel cells ($\mu\text{-SOFC}$), and gas sensors, demands the synthesis of the materials as thin films. Therefore, there has been an extensive research about the preparation and characterization of BNO films deposited by both chemical^[8g-i,14] and physical vapor (PVD) deposition techniques. Most of these works have evaluated the dielectric response of the films for applications as the dielectric layer in capacitors.

An advantage of the PVD methods is the high purity of the films, because the adatoms come directly from the target through a vacuum atmosphere without the use of any chemical precursor. Chattopadhyay et al.^[15] were pioneers in the preparation of BiNbO_4 films by PVD using pulsed laser deposition (PLD) to ablate a BiNbO_4 target. Crystalline $\alpha\text{-BiNbO}_4$ films were obtained heating the substrates above 600 °C, and they observed ferroelectric behavior when the thickness was thinner than 600 nm. Later, Park et al.^[8c] ablated a Bi_3NbO_7 target to obtain amorphous Bi_3NbO_7 films on polymeric substrates by PLD at room temperature (RT); the authors evaluated the dielectric properties of the films concluding that the films could be used as the dielectric layer for capacitors implanted in printed circuit boards at temperatures below 200 °C. Cho et al.^[8f] used radio-frequency (rf) magnetron sputtering to prepare different BNOs films from a single $\text{Bi}_5\text{Nb}_3\text{O}_{15}$ target. The applied power was fixed and the deposition temperature was varied from RT to 600 °C. They obtained amorphous films containing $\text{Bi}_5\text{Nb}_3\text{O}_{15}$ nanocrystallites at temperatures lower than 300 °C, while crystalline $\text{Bi}_5\text{Nb}_3\text{O}_{15}$ films were obtained between 300 and 550 °C. At higher temperatures, the BiNbO_4 phase was obtained and the change in the composition was attributed to the facile volatilization of Bi. Seong et al.^[16] prepared BNOs films also starting from a $\text{Bi}_5\text{Nb}_3\text{O}_{15}$ target but using PLD and varying the deposition temperature, the O_2 pressure, and the Mn concentration. Similarly to previous works, the substrate temperature had a strong effect on the structure and composition. The films deposited below 400 °C were amorphous and the Bi_3NbO_7 phase was obtained at 400 °C. Meanwhile the $\text{Bi}_5\text{Nb}_3\text{O}_{15}$ phase was obtained between 400 and 700 °C and at 700 °C the loss of Bi content due to the evaporation of Bi_2O_3 led to the formation of the BiNbO_4 phase. The effect of the oxygen pressure was mainly observed in the electrical properties (leakage current and breakdown voltage) due to a different fraction of O vacancies present in the films. Szwachta et al.^[17] deposited films of $\text{II-Bi}_3\text{NbO}_7$ by PLD onto single-crystal sapphire substrates heated at different temperatures and starting

from a single target with the same composition. The results showed that it was possible to obtain pure cubic Bi_3NbO_7 at 350 °C and the films were stable after ex situ annealing up to 900 °C. Nishimura et al.^[18] reported the use of the co-sputtering method using two independently driven Nb and Bi targets under a reactive $\text{Ar}:\text{O}_2$ atmosphere at 500 °C. It was found that the addition of Bi (9.8–53 at%) into the crystalline Nb_2O_5 led to amorphous films with different Bi–Nb bonding and optical characteristics. However, no crystalline BNOs phases were reported.

The objective of the present work is to show that using the co-sputtering method is possible to obtain the different crystalline BNOs phases, either as-deposited or after annealing. The advantage of dual co-sputtering is the synthesis of different BNOs phases without going through the fabrication of expensive targets of fixed composition, which might require the use of extreme conditions in order to make them.^[16] The use of co-sputtering has been extensively reported either using a mixed-composition target or individual targets. It has been shown to be a feasible method to dope metal oxide coatings,^[19] or to obtain specific compounds such as Bi_2Te_3 ,^[20] monoclinic BiVO_4 ,^[21] or $\text{Cu}_2\text{ZnSnS}_4$.^[22] It has also been used to the synthesis of nanocomposite coatings,^[23] allowing the stabilization of specific phases^[21,24] or preferred growth orientations,^[25] as well as the deposition of ternary and quaternary compounds.^[26]

In our previous work,^[27] the synthesis and photocatalytic properties of $\text{Bi}_5\text{Nb}_3\text{O}_{15}$ thin films deposited using the referred dual confocal co-sputtering method was proved. The present paper reports, not only a single phase, but a systematic study of the different phases which can be obtained of the complex $\text{Bi}_2\text{O}_3\text{--Nb}_2\text{O}_5$ system using co-sputtering and their optical properties.

2. Experimental Section

2.1. Preparation of the Films

The different BNOs were synthesized using a reactive magnetron co-sputtering system with two targets independently driven: $\alpha\text{-Bi}_2\text{O}_3$ (purity 99.9%) and metallic Nb (purity 99.95%), both of 2" diameter; the oxide target was energized by a radiofrequency (rf) supplier and the metallic target by a direct current (DC) supplier, both targets were sputtered simultaneously. The geometric configuration of the targets–substrates system and the rotation to warrant the homogeneity of the films were the same as those used in the previous work.^[27] The rf-power applied to the Bi_2O_3 target was fixed at 30 W (1.5 W cm^{-2}), while the DC power applied to the Nb target was varied between 20 and 150 W. The deposits were done under an $\text{Ar}:\text{O}_2$ reactive atmosphere with a fixed gas ratio of volumetric flow (standard cubic centimeter per minute, sccm) 16:4, and the work pressure was 0.7 Pa. The films were deposited simultaneously on two substrates: silicon (100) and Corning[®] 7059 glass pieces of 1×1 and $2 \times 2 \text{ cm}^2$, respectively. Two series of samples were deposited: in the first one or preliminary (series 1), the power applied to the Nb target was varied in the whole 20–150 W window and the substrates were heated at 150, 200, and

250 °C for 30 min before deposition. This series was used mainly for a structural-composition characterization in order to determine the conditions that led to crystalline BNOs phases. Moreover, since some films were amorphous, we explored the annealing requirements to induce the crystallization of the amorphous films and evaluate the possible changes in composition before and after post-annealing.

Then, a second set of samples (series 2) were produced using selected values from the analysis of the first samples. The selected powers applied to the Nb target were 20, 30, 50, 70, and 100 W, equivalent to 1, 1.5, 2.5, 3.4, and 4.9 W cm⁻², respectively. The substrate temperature (T_s) was fixed at 150 °C and the deposition time at 30 min.

The samples of this series were then labeled as BNO-X, where X is the power applied to the Nb target, as shown in Table 1.

2.2. Characterization

The Nb content of the as-deposited and the annealed films was determined by the energy-dispersive X-ray spectroscopy (EDS) analysis, using a system attached to the JEOL 7600F field emission-scanning electron microscope (FE-SEM).

The crystallinity of the films was verified by X-ray diffraction (XRD) using a Rigaku diffractometer, model Ultima IV, equipped with Cu $K\alpha$ radiation, in Bragg-Brentano mode, acquisition step 0.02°, scanning speed 1° min⁻¹ and the 10–60° diffraction angle (2θ) range. The amorphous as-grown films (series 1) were submitted to high temperature (HT) in situ XRD measurements in air using the HT attachment of the Rigaku equipment for the samples deposited on Si. A heating rate of 10 °C min⁻¹ was programmed, the treatment temperatures were 200, 300, 400, 500, 600, and 700 °C and the holding time was 1 h for each temperature. The recording conditions at each temperature were: acquisition step 0.02°, scan speed 2° min⁻¹ and 2θ range 10–60°; the data acquisition started after the first

half hour at the holding temperature. The cooling down was at natural rate, and another scan was recorded when the treated sample reached RT. From these results, the more suitable temperature for annealing was determined as 600 °C. The amorphous films (series 2) were annealed into a tubular furnace at 600 °C for 2 h and in static air for samples deposited on both substrates.

For series 2, the film characterization was done for the samples deposited on glass after the confirmation that the structure was the same, independently of the substrate used. The identification of the crystalline phases, in the as-grown and annealed films, and the calculation of the lattice parameters, phase weight proportion (by the reference intensity ratio RIR method^[28]) and crystalline domain size (by the Halder–Wagner method^[29]) were done using the PDXL2[®] software. The software has an algorithm to search the best match between the experimental and reported data, thus it selects the candidate phase considering the minor possible figure of merit value. In addition, the structure was verified by micro-Raman spectroscopy using an En-Spectra R532 spectrometer with laser wavelength 532 nm.

The thickness and roughness of the films was measured using a Veeco model Dektak 150 stylus profilometer. In addition, the chemical composition and the oxidation states of Bi and Nb were determined by X-ray photoelectron spectroscopy (XPS), using a Physical Electronics VersaProbe II system equipped with a scanning XPS microprobe. The measurements were done under ultrahigh vacuum of 4×10^{-8} Pa, and the X-ray source was of Al $K\alpha$ ($h\nu = 1486.6$ eV). The low-resolution spectra were recorded using 117.4 eV as step of energy, and the high-resolution spectra at 11.75 eV. Moreover, the low-resolution spectra were measured before surface cleaning, in order to correct the position of the peaks of all the present elements respect to the adventitious C1s peak (284.8 eV). The high-resolution spectra were sequentially recorded after the cleaning through the Ar⁺ ions bombardment with energy of

Table 1. Notation of the samples according the power applied to the Nb target and the summary of the data of each film obtained from the EDS/XPS and XRD measurements.

Sample	Nb power [W]	Nb content [at%]	Nb/Bi atomic ratio	Identified phases [by XRD + EDS/XPS]	Lattice parameters [Å]	Calculated density [g cm ⁻³]	Crystalline domain size [nm]
BO	–	0	0	δ -Bi ₂ O ₃	$a = b = c = 5.587$	8.8736	13
BNO-20	20	5.1	0.17	Solid Solution (S.S.) with 5.1 at% Nb and type II structure	$a = b = c = 5.546$	8.5527	18
BNO-30	30	6.6	0.25	S.S. with 6.6 at% Nb and type II structure	$a = b = c = 5.524$	8.4874	14
BNO-50	50	9.2	0.39	II-Bi ₃ NbO ₇ structure or S.S. with 9.2 at% Nb.	$a = b = c = 5.516$	8.2235	20
BNO-70-TT ^{a)}	70	12.5	0.6	Bi ₅ Nb ₃ O ₁₅	$a = 20.94,$ $b = 5.31,$ $c = 5.46$	8.554	52
BNO-100-TT ^{a)}	100	16.1	0.92	α -BiNbO ₄ (76 wt%) β -BiNbO ₄ (24 wt%)	$a = 5.663,$ $b = 11.711, c = 4.974$ $a = 7.62,$ $b = 5.55, c = 7.92$	7.385	35

^{a)} TT means thermal treatment (annealing).

0.5 kV during 20 s, the total sputter time was 60 s divided in three intervals of 20 s each one. The current density of the ion beam was 55.6 nA mm^{-2} . The data was analyzed using the Multipak© version 9.6.0.15 software.

The optical properties were evaluated using an UV-Visible-NIR JASCO V670 spectrometer equipped with an integrating sphere to measure the specular transmittance and reflectance spectra, the geometric configuration allowed the spectra acquisition from the same area of the sample. The refractive index (n), extinction coefficient (k) and absorption coefficient (a) spectra, and the optical gap (E_g), were calculated from the fitting of theoretical models to the experimental data using the CODE[®] software. The geometric model used for determining the optical properties includes a bottom homogenous layer and porous layers with different proportion of voids. The layer model was, from bottom to top: Air/Glass/Film/Film + Air/Air. The optical properties of the glass substrate were estimated by a direct measurement and modeling of the clean glass substrate. The compose Film + Air layer was modeled using the Bruggeman effective medium approximation,^[30] where the volume fraction of each component is a fitting parameter and this layer simulate the porosity and roughness. The Tauc-Lorentz model^[31] and Kim oscillators^[32] were used to parameterize the optical properties of the films. The fundamental optical transition (optical gap) was assumed indirect, that is, from the linear region extrapolation of $(ah\nu)^{1/2}$ versus the photon energy.

3. Results and Discussion

3.1. Series 1

Series 1 was used to determine the amount of Nb that could be added to the Bi_2O_3 films using the different powers applied to the Nb target (20–150 W) and its effect on the film-structure as a function of the substrate temperature (150–250 °C).

The results showed that the Nb content increases linearly with the power applied to Nb target (Figure S1 of the Supporting Information) from 6 to 24.1 at%, corresponding to powers between 20 and 150 W, respectively. Since the maximum Nb content for the best-known BNOs phases is 16.67 at% found in the BiNbO_4 compound, the samples deposited at 150 W were not considered for series 2.

The results indicate that powers above 50 W led to amorphous films independently of the substrate temperature as shown in Figure 1, which shows the XRD patterns for the different powers and T_s . The patterns of the samples deposited from 0 W up to 50 W show that these films were crystalline and the peaks could be indexed with BO or BNOs phases. Above 50 W, the films were considered amorphous, because a broad single peak appears in each pattern, and this does not allow identification of any compound or phase. This behavior was observed for the three substrate temperatures suggesting that the power applied to the Nb target was the determining deposition condition for the crystallinity of the films, and probably on the phases present in the films, under the used T_s range.

The evolution of the structure during annealing of the amorphous samples is shown in Figure 2. The sample deposited

at 70 W applied to the Nb target (Figure 2a), remained amorphous up to 300 °C, then, between 400–500 °C, the predominant phase is Bi_3NbO_7 , and at 600–700 °C, the $\text{Bi}_5\text{Nb}_3\text{O}_{15}$ phase was obtained. This phase was retained after cooling. Figure 2b shows that the sample deposited at 100 W, the present patterns corresponding to polymorphs of the BiNbO_4 compound at 600 °C and that such phases, remain after cooling. The film deposited applying 150 W to the Nb target crystallized in a Nb-rich phase. The XRD peaks were indexed as the pseudo-hexagonal TT- Nb_2O_5 phase (data not shown), thus this power was discarded for series 2. Analysis of the results indicated that 600 °C was an annealing temperature to obtain a crystalline BNO phase.

The annealing led to a slight increment in the Nb content of about 7% (Figure S1). These results indicate that the composition of the films was determined mainly by the power applied to the Nb target; meanwhile the structure depends on both; the power and the temperature used to crystallize the film.

One plausible explanation for the amorphization of the films as the Nb content was increased is due to the influence of the nature of the Nb_2O_5 . A phase diagram of the Nb_2O_5 shows that this oxide is amorphous from RT up to 400 °C.^[33] Similarly, Nb_2O_5 thin films are amorphous at the same temperature range, but they could crystallize by post-annealing at 500 °C or using T_s of 500 °C.^[34] On the other hand, as we have shown in a previous work,^[35] BO is crystalline even at growth temperatures as low as 125 °C and it undergoes changes into different crystalline phases as the temperature increases, but it stays always crystalline.

3.2. Series 2

Based on the results showed for series 1, the powers applied to the Nb target, T_s and annealing temperature were selected to deposit another series of films on glass substrates in order to measure the optical properties of the crystalline and well-identified BNO polymorphs. The results from the characterization of this second series of films are presented below.

3.2.1. Films Growth and Composition

Figure 3 shows the surface morphology of the crystalline (a–d) as-grown films and the crystalline films by post-annealing (e,f). The insets in Figure 3 show the cross-sectional morphology of the films. From the film cross-sectional images, it was possible to estimate the thickness, which is in good agreement with the profilometry data (Figure 4). The surface morphology of the as-deposited crystalline films (BO, BNO-20, BNO-30, and BNO-50) looks similar among them: granular and uniform. These cross-sectional micrographs show that the sputtered deposited films are compact with a columnar growth. The surface and cross-sectional morphology of the annealed films (BNO-70-TT and BNO-100-TT) is different to the others because the process of crystallization was different. In these last samples, some defects could be observed, such as porosity and cracks, probably due to the atomic rearrangement and different expansion coefficients of the film and substrate materials.

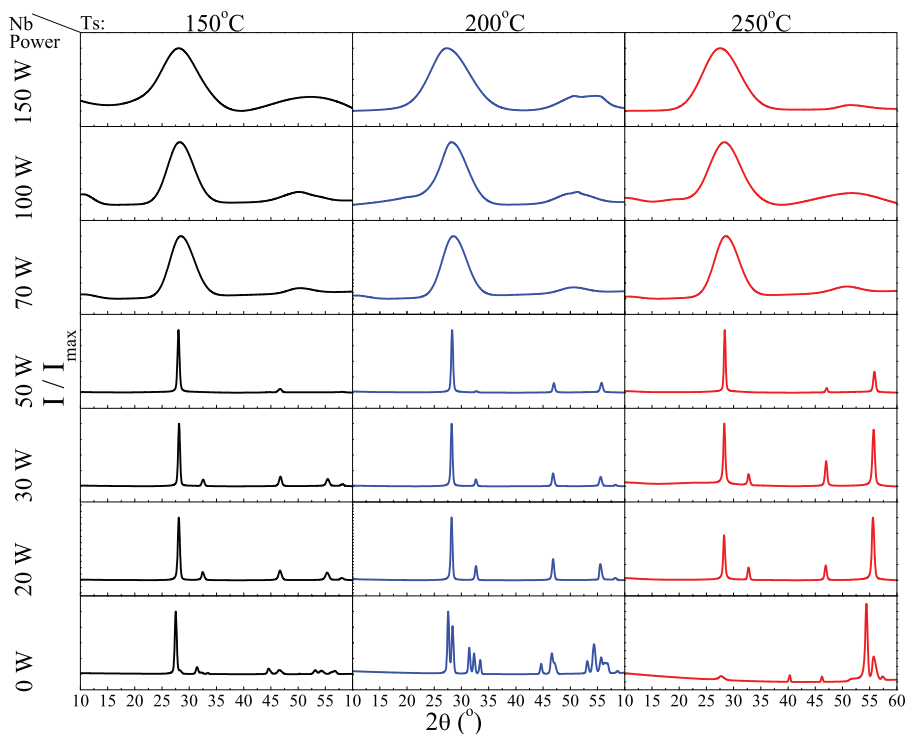


Figure 1. Preliminary structural evaluation of the as-grown films deposited varying power applied to Nb target and the pre-heating substrate temperature.

The Nb content obtained from EDS analysis using the Bi, Nb, and O fractions, as well as the thickness and deposition rate are shown in Figure 4 as a function of the power applied to the Nb target; data also included in Table 1. It can be seen that there is a

relatively good agreement between the profilometry and SEM data, showing that both the film thickness and deposition rate increased linearly with the power applied to the Nb target. Additionally, the thickness variation of the BNO-70-TT and

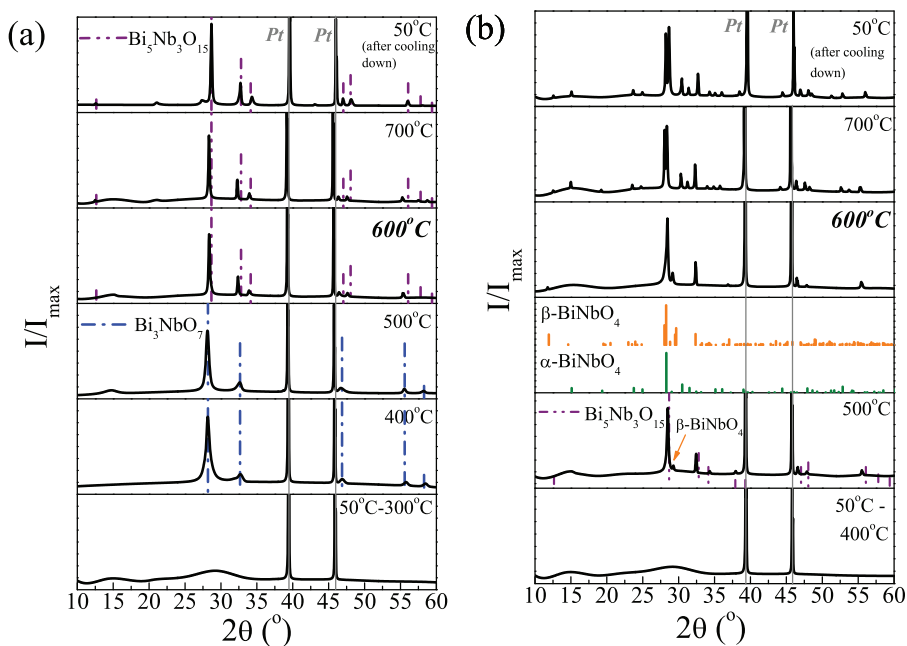


Figure 2. High temperature XRD evaluation of the structural evolution of series 1 films deposited applying: a) 70 W and b) 100 W to the Nb target. The peaks located at 39 and 46° correspond to the material of the sample holder, that is, platinum (Pt).

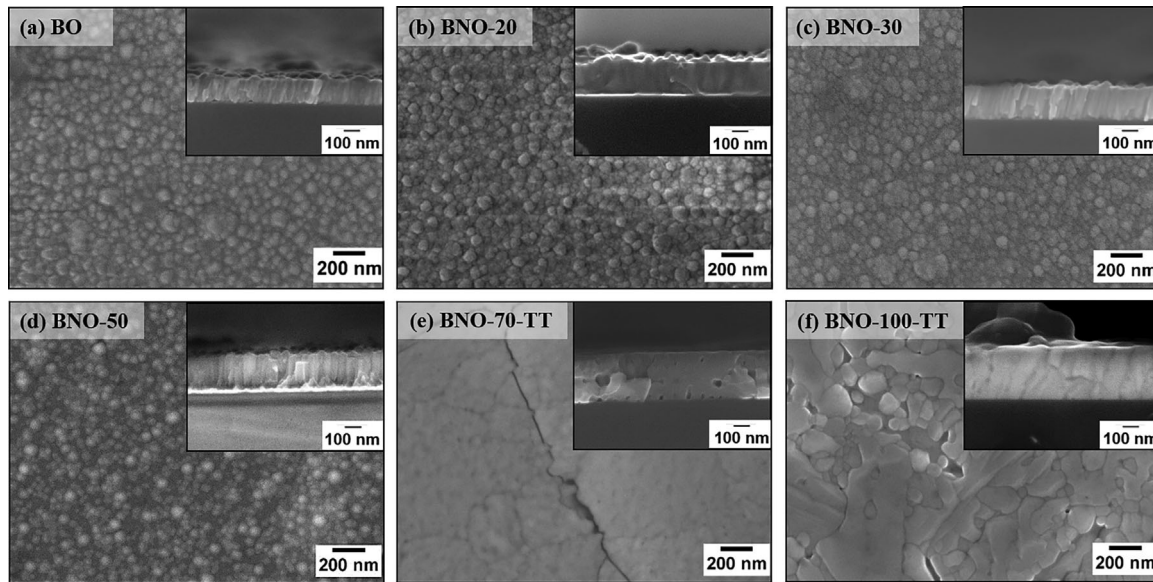


Figure 3. Surface morphology of the crystalline films both as-grown a–d) and after the annealing, TT e and f). Inset: cross-sectional micrographs of the films.

BNO-100-TT films before and after annealing was negligible. As described by series 1, the Nb content increased linearly with the power applied to the Nb target, from 5.1 at% at 20 W to 16.1 at% at 100 W. On the other hand, the roughness of the films was between 4 and 17 nm, the films with higher roughness were those that grew crystalline.

The bonding characteristics were analyzed by XPS. The XPS high-resolution spectra of Bi4f and Nb3d orbitals are shown in **Figure 5** for three Ar⁺ erosion times: 20, 40, and 60 s. The position of the peaks was corrected respect to the C1s signal position (284.8 eV). The top-row spectra in Figure 5 show that all

films presented the spin-orbit doublet corresponding to Bi4f_{7/2} and Bi4f_{5/2} orbitals. The binding energy (BE) of the Bi4f_{7/2} photoelectrons is around 159 eV and the 4f doublet separation (DS) is 5.3 eV, in good agreement with BE and DS reported for Bi³⁺ according to the database.^[36] This doublet is the unique one for BO, BNO-20, BNO-30, and BNO-50 samples, meaning that no other chemical environments or Bi oxidation states were present. However, the Bi 4f spectra for the annealed samples (BNO-70-TT and BNO-100-TT) show a second and weaker doublet at lower energies. The chemical shift separation between the two Bi4f_{7/2} peaks is 2 eV, which indicates that the weaker doublet corresponds to metallic Bi (Bi⁰),^[36] but present in small proportions. The bottom-row spectra in Figure 5 show that there is a unique Nb3d doublet for all films, which corresponds to Nb3d_{5/2} and Nb3d_{3/2} orbitals. The peak of the Nb3d_{5/2} orbital is positioned around 207 eV, this value is the characteristic binding energy of the Nb⁵⁺ oxidation state, and the spin-orbital splitting of 2.72 eV is in agreement with the literature.^[36] The spectra indicate that the films belong to the Bi₂O₃–Nb₂O₅ pseudo-binary system because Bi and Nb have predominant oxidation states identified as 3⁺ and 5⁺, respectively.

The presence of the metallic state is possibly due to the reduction of Bi during the post-annealing,^[35,37] and most probably, the metallic bismuth is located in the tridimensional defects originated by the annealing (porous and cracks). Under the erosion current conditions, the presence of the metallic bismuth signal was not a consequence of the erosion process such as it has been reported for others transition metal oxides, for example, Zr^[38] and V.^[39] However, it is worth to mention that longer cleaning times (>3 min) and higher Ar⁺ ion beam energies (>1 kV) led to strong modification of the Bi bonding environment, showing a higher proportion of the reduced state (see Figure S4 of the Supporting Information). In contrast, the Nb–O bond seems very stable regardless of the cleaning sputter conditions and thermal treatments. The XPS elemental

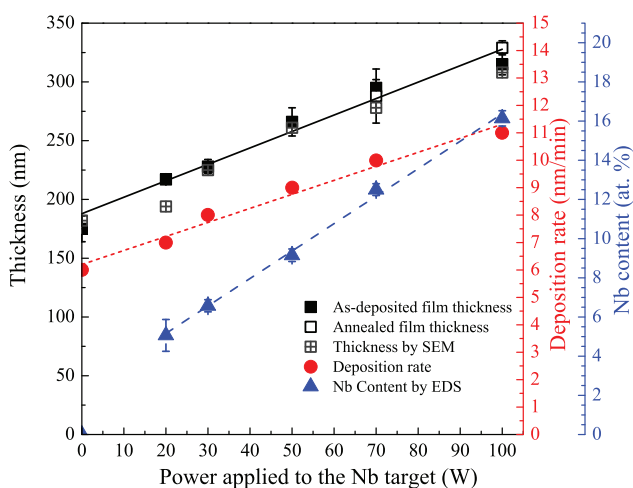


Figure 4. Thickness, deposition rate, and Nb content of the films of the second series as function of the applied power to the Nb target. The Nb content was determined by EDS. The solid line, short dashed, and dashed lines represents the linear trend of the film thicknesses ($R^2 = 0.965$), deposition rate ($R^2 = 0.974$), and Nb content ($R^2 = 0.994$), respectively.

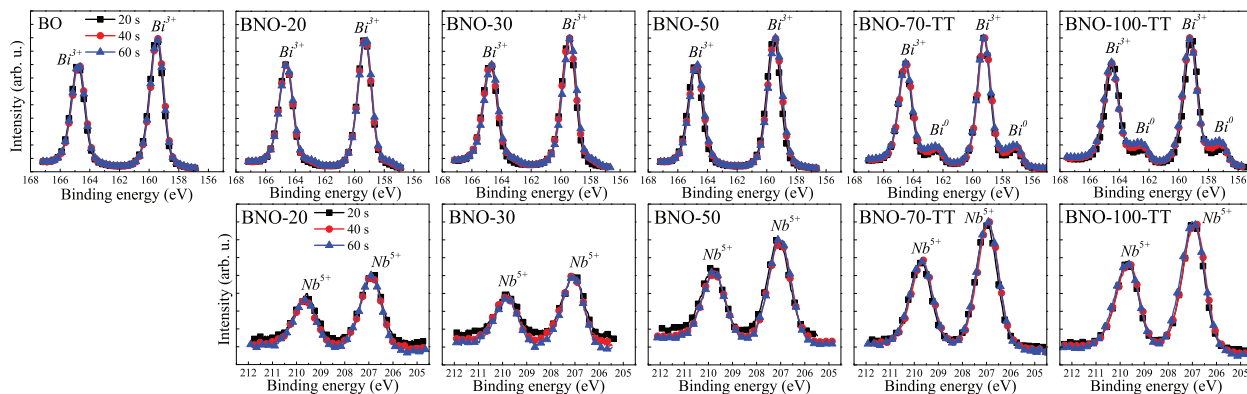


Figure 5. XPS high resolution spectra of Bi4f and Nb3d orbitals, recorded after Ar⁺ ion cleaning each 20 s until 60 s.

composition was obtained from the spectra measured after the 60 s of erosion in order to warrant that the composition of the film is reported, instead of the surface layer.

The composition ratio (Nb/Bi atomic ratio) obtained from the XPS analysis is shown in **Figure 6** as a function of the power applied to the Nb target, which shows a good agreement with the EDS data. This trend is expected because the Nb incorporation is linearly proportional to the applied power (**Figure 4**), and the Bi content must be suitable to compensate the oxygen atomic fraction of the different phases belonging to the Bi₂O₃-Nb₂O₅ pseudo-binary system.

3.2.2. Films Structure

Figure 7 shows the XRD patterns and proper phase identification corresponding to the crystalline films, both (a) from deposition and (b) after the annealing for the films deposited on the Corning 7059[®] glass. In all patterns, the characteristic peaks of

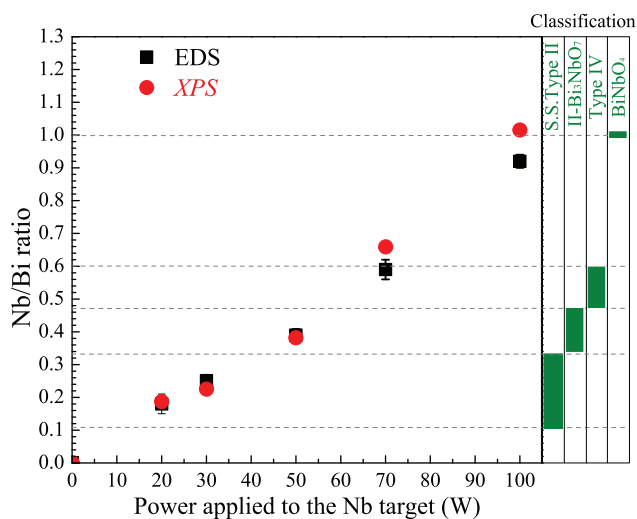


Figure 6. Nb/Bi ratio as function of the power applied to the Nb target. The Nb/Bi ratio ranges according to the structure classification are included.

the different phases are present, which means that the films are polycrystalline. Moreover, the intensity relation between the diffraction peaks is similar to that of the powder pattern suggesting that the films are not textured. **Figure 7a** shows that the as-grown crystalline film without Nb (BO) has the fluorite structure of the cubic δ -Bi₂O₃ phase and similarly, after addition of low concentrations of Nb (BNO-20, BNO-30, and BNO-50), the patterns agree with the fluorite-type structure, which is related to the type II structure proposed by Zhou et al.^[10] The increment of the Nb content originated a shift of the diffraction peaks to higher angles (see **Figure S2** of the Supporting Information) due to the shrinking of the unit-cell as a consequence of the substitution of Bi³⁺ for the Nb⁵⁺ ion, which has a lower atomic radius. An approximate estimation of the lattice parameters using the diffraction angles reflects the decrease of the lattice parameters of the type II solid solutions as shown in **Table 1**. The phases in the as-grown crystalline films are identified as δ -Bi₂O₃ for the BO sample (00-52-1007), solid solutions with type II structure in the BNO-20 and BNO-30 samples (00-033-0210) and II-Bi₃NbO₇ niobate (01-089-5564) for the BNO-50 film. The ICDD No. 00-033-0210 card corresponds to Bi_{1.7}Nb_{0.3}O_{3.3}, which is a BNO solid solution.

Figure 7b shows the identification of the crystalline phases of the BNO-70-TT and BNO-100-TT films, resulting from the post-annealing at 600 °C. The orthorhombic Bi₅Nb₃O₁₅ niobate was identified in the BNO-70-TT sample using the data of the ICSD #245707 card. Meanwhile, a mixture of polymorphs of BiNbO₄ was identified in the pattern of the BNO-100-TT sample, using the ICDD No. 01-082-0348 and 01-071-1518 cards for α - and β -BiNbO₄ phases, respectively. The results are in good agreement with the observed phases during the annealing of the series 1 sample (**Figure 2**), even though that different substrates were used. Moreover, for all the deposited samples, the structure obtained before or after annealing was not dependent on the substrate, as can be confirmed in **Figure S3**. The list of diffraction peaks of the BNO-70-TT and BNO-100-TT films, with their corresponding database references and indexes, is shown in **Table 2**. Only the angles with a good match ($\leq 0.14^\circ$) respect to experimental peaks are shown for α - and β -BiNbO₄ phase.

The orthorhombic α -BiNbO₄ phase is predominant (76 wt%) and the rest of the weight corresponds to the triclinic β -BiNbO₄

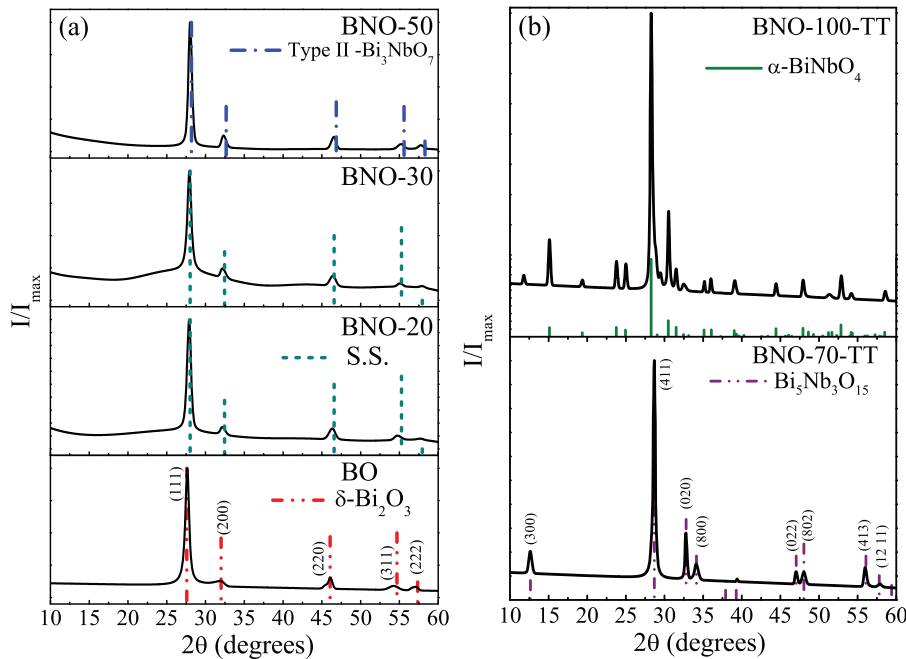


Figure 7. Identification of the present phases in the crystalline films both a) as-grown and b) after the annealing, according to the XRD evaluation.

phase. The summary of the data extracted from the XRD patterns, such as the lattice parameters and the crystalline domain size, are shown in Table 1.

The production of crystalline films of $\text{Bi}_5\text{Nb}_3\text{O}_{15}$ and α - + β - BiNbO_4 has also been reported using T_s between 450 and 600 °C.^[8f,15,16,40] Besides, it has been reported that the production of $\text{Bi}_5\text{Nb}_3\text{O}_{15}$ and BiNbO_4 powders requires calcination and sintering temperatures higher than 800 °C,^[7g,8c,41] the lowest temperature reported for the synthesis of the $\text{Bi}_5\text{Nb}_3\text{O}_{15}$ in powder is 600 °C,^[42] which is the same as the crystallization temperature used in this work. Notwithstanding that these temperatures appear to be very high for considering these compounds as the dielectric layer on printed circuit boards, other nitrides, and oxides with excellent dielectric properties have crystallization temperatures even higher than 900 °C.^[8f,43] Therefore, the synthesis demonstrated here at 600 °C of these crystalline niobates might be of interest for microelectronic applications.

Even though a film of pure α - or β - BiNbO_4 phase was not produced, it is interesting to note that the triclinic β - BiNbO_4 was obtained at lower temperature than its stability temperature in bulk (>1020 °C), similarly to the polymorphic films reported by Seong et al.^[16] The stabilization of high temperature or metastable phases is one of the virtues of the atomic aggregation deposition techniques, where the growth process is not under thermodynamic equilibrium, and the kinetics of growth dominates the process, such as has been observed for the δ - Bi_2O_3 phase^[44] which in bulk is stable between 730 and 825 °C but can be obtained at RT as a thin film. Furthermore, Zhai et al.^[41a] reported the existence and stability of pure β - BiNbO_4 powder at temperatures below 1020 °C, that is, 700 °C. They synthesized this phase by the chemical citrate method, and that process involved sequential thermal treatments for 3 h each one. Apparently this phase could be stabilized at temperatures below

1020 °C, reported as the transition temperature by Roth and Waring,^[9] even using processes close to the thermodynamic equilibrium.

The structure of the films was also evaluated using Raman spectroscopy. **Figure 8a–f** show the Raman spectra of the films. A unique broad band is observed around 626 cm^{-1} in the Raman spectrum of the δ - Bi_2O_3 (Figure 8a), this signal has been reported by other authors as a signature of the δ - Bi_2O_3 phase at close frequencies between 621^[45] and 618 cm^{-1} .^[46] Figure 8b–c show the Raman spectra of the films with different concentrations of Nb and fluorite-like structure, their spectra have a similar band to the δ - Bi_2O_3 spectrum but wider and shifted toward higher frequencies. Ermakova et al.^[45] attributed the presence of a unique wide band to the relaxation of the selection rules in the disordered cubic structure of BO, which is also obtained for these Nb solid solutions. The intensity of the band decreases as the Nb content increases, until it almost disappears for the BNO-50 sample (Figure 8d). This is probably a consequence of the ordering of the anionic and cationic sublattices when the Nb^{5+} cations substitute the Bi^{3+} cations, the density of vacancies tends to decrease and the coordination of the metallic cations changed.^[6e,45]

The Raman spectrum of the BNO-70-TT is shown in Figure 8e and was firstly published in our previous work^[27] where we demonstrated theoretically that the signals located at the frequencies: 164, 201, 435, 562, and 852 cm^{-1} , are characteristic of the mentioned niobate. We proposed that the main band at 852 cm^{-1} can be considered as the fingerprint of the $\text{Bi}_5\text{Nb}_3\text{O}_{15}$ phase. For the BNO-100-TT sample, the Raman spectrum (Figure 8f) show mainly signals from the orthorhombic polymorph, α - BiNbO_4 . However, one minor peak associated to the triclinic β -phase could also be observed, agreeing with the XRD results (top of Figure 7b and Table 2). The band positions of

Table 2. List of 2θ angle positions of the experimental XRD peaks of annealed films and the reported peaks of the identified phases with their respective Miller indexes.

2θ [°]	Plane Miller indexes of		2θ [°]		Plane Miller indexes of		
	BNO-70-TT	$\text{Bi}_5\text{Nb}_3\text{O}_{15}$ ^{a)}	BNO-100-TT	$\alpha\text{-BiNbO}_4$ ^{b)}	$\alpha\text{-BiNbO}_4$	$\beta\text{-BiNbO}_4$ ^{c)}	
12.60	12.63	(3 0 0)	11.78			11.92	(1 0 0)
28.66	28.653	(4 1 1)	15.10	15.11	(0 2 0)		
32.71	32.707	(0 2 0)	19.38	19.36	(0 1 1)		
34.04	34.120	(8 0 0)	23.77	23.76	(1 0 1)		
39.38	39.267	(5 2 0)	24.98	24.96	(1 1 1)		
46.96	46.976	(0 2 2)	28.25	28.28 ^{d)}	(1 2 1)	28.26 ^{d)}	(2 1 0)
48.01	48.031	(8 0 2)	28.85			28.81	(1 -1 2)
55.92	55.995	(4 1 3)	29.46			29.5	(2 0 2)
57.9	57.773	(12 1 1)	30.51	30.5	(0 4 0)		
	59.325		31.48	31.51	(2 0 0)		
			32.44	32.45	(2 1 0)		
			35.17	35.12	(2 2 0)	35.18	(1 -2 0)
			35.97	36.06	(0 0 2)		
			39.06	39.03	(1 4 1)		
			44.40	44.43	(2 4 0)		
			47.91	47.93	(0 4 2)		
			51.30			51.29	(2 -1 4)
			52.85	52.85	(1 6 1)	52.8	(4 -1 0)
			54.14	54.15	(3 2 1)	54.18	(3 -2 -1)
			58.53	58.5	(1 1 3)		

^{a)} Values calculated from the ICSD #245707 card data; ^{b)} ICDD No. 01-082-0348; ^{c)} ICDD No. 01-071-1518 cards; ^{d)} These angles correspond to the position of the most intense peak of both BiNbO_4 polymorphs.

$\alpha\text{-BiNbO}_4$ are: 139, 158, 198, 254, 273, 336, 370, 382, 426, 537, 625, and 734 cm^{-1} ; these positions match the reported values by Ayuub et al.^[47] and Zhai et al.^[41a] The weak signal located at 687 cm^{-1} can be associated to $\beta\text{-BiNbO}_4$ (indicated with a dashed circle in Figure 8f), since it coincides with the report of Zhai et al.^[41a] Nevertheless, many bands of both polymorphs overlap making difficult a more precise identification. In general, the identification of the phases through Raman spectroscopy agrees very well with the XRD results.

A summary of the structure and composition results can be observed in Figure 6, it includes the Nb/Bi atomic ratio and the structure according to the specifications given in Section 1. It can be observed that it was possible to obtain most of the phases of the BNO system: solid solutions based on $\delta\text{-Bi}_2\text{O}_3$, $\text{II-Bi}_3\text{NbO}_7$, $\text{Bi}_5\text{Nb}_3\text{O}_{15}$, and the BiNbO_4 phase. A critical sample is the BNO-50 film (9.2 at% of Nb), which has a composition close to the Bi_3NbO_7 niobate (9.09 at%), so it can be considered as a representative compound of the type III structure but it could also be identified as a type II structure according to literature.^[6d,11] Nevertheless, the type-II and the solid solutions present the same cubic structure, making impossible a complete identification based on the XRD data. Moreover, considering that for vapor deposited coatings, the solubility limits are not strictly equal to the bulk data,^[48] sample BNO-50 could also be considered as a solid solution even that the composition is

beyond the limits defined by Zhou et al.^[10] On the other hand, the Raman spectrum of the Bi_3NbO_7 compound has not been reported yet, then it is not possible to use the Raman spectra to verify the presence of this niobate in the BNO-50 sample; some other advanced techniques should be used.

The fact that the BO, BNO-20, BNO-30, and BNO-50 have a type II structure, implies that the fluorite-like structure can be stabilized and preserved at RT adding Nb up to 9.2 at%. This stabilization of the fluorite structure is of interest for ionic conductivity applications and was extensively studied in bulk samples aiming to keep the fluorite structure down to RT while preserving the high ionic conductivity.^[5a,6a,49] For thin films, Gomez and Rodil^[50] showed that it is possible to keep the fluorite structure of the BO films by forming solid solutions with Ta, W, or Al; interestingly, the ionic conductivity was also preserved.^[50]

3.2.3. Optical Properties

Regardless of the interest on the low-frequency dielectric properties of the BNO films and the ionic conductivity, few works have assessed the UV-Visible dielectric response of the BNO films.^[51] The reported bandgaps were studied in relation to the photocatalytic properties of the BNO phases and estimated from diffuse reflectance measurements using compact powders.

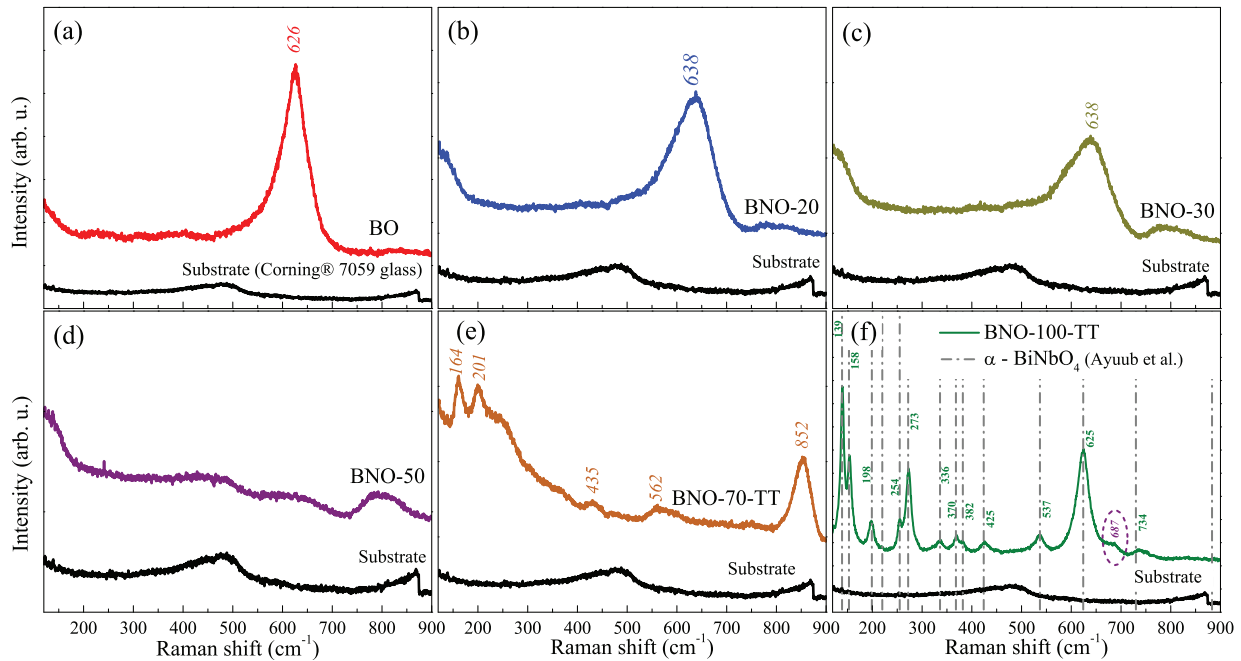


Figure 8. Raman spectra of the crystalline films: a–d) as-grown, and e and f) after annealing. In f) the dashed circle indicates a weak signal apparently of β - BiNbO_4 .

Therefore, the Kubelka–Munk function was used, which does not allow the calculation of neither the absorption coefficient (α) (related to the extinction coefficient (k)) nor the refractive index (n). In this work, we have obtained a complete characterization of the UV-Visible response of the different BNO phases by a careful modeling of both transmittance and reflectance spectra.

Figure 9 shows the experimental and model transmittance (T) and reflection (R) spectra of (a–d) the as-grown crystalline and (e, f) annealed films, which were measured by UV-Visible-NIR spectrometry. It can be observed that the drop in the transmittance is shifted to the blue as the Nb content increases, which implies that the optical gap increases. Similarly, the increment of the number of fringes in the transparent region of the spectra indicates that the films are thicker as the Nb content increases, in agreement with the result shown in Figure 4.

The experimental spectra were modeled using the layers described in the experimental section, where the dielectric function was determined combining the Tauc–Lorentz model^[31] and Kim oscillators^[32] models. The first model proposed the junction of the Lorentz oscillators and the Tauc method to calculate the optical gap of amorphous semiconductors; the dielectric imaginary part $\varepsilon_i(E)$ is calculated as shown in Equation (1) and the real part $\varepsilon_r(E)$ is determined by the Kramers–Kronig integral:

$$\varepsilon_i(E) = \begin{cases} \sum_n \frac{1}{E} \frac{A_n E_{on} C_n (E - E_{TL})^2}{[(E^2 - E_{on}^2) + C_n^2 E^2]}, & E > E_{TL} \\ 0, & E \leq E_{TL} \end{cases} \quad (1)$$

where n , E , A , C , and E_0 are the number of oscillators, photon energy, amplitude, broadening, and position of the peak (or

oscillator), respectively. The E_{TL} , also known as the Tauc–Lorentz gap, is the energy at which k begins to rise. The Kim oscillator model^[32] is an extension of the simple harmonic oscillator model, and it allows a continuous shift of the line shape between a Gaussian and a Lorentzian profile, see Equation (2) and (3):

$$\hat{\varepsilon}(\omega) = 1 + \frac{A\omega_0^2}{\omega_0^2 - \omega^2 - i\omega\tau(\omega)} \quad (2)$$

$$\tau(\omega) = \gamma \exp\left(-\frac{1}{1+s^2} \left(\frac{\omega - \omega_0}{\gamma}\right)^2\right) \quad (3)$$

where ω , ω_0 , A , γ , and s are the frequency, resonance frequency, amplitude, damping of the oscillator, and the Gaussian–Lorentz shift, respectively. In both models the E_0 and ω_0 indicate the electronic interband transition energies; A represents the transition probability and C or γ the half-life time of the excited electronic state.

The fitting parameters are shown in Table S1 of the Supporting Information. The parameters indicate the resonance energy of the fundamental and interband transitions, the dielectric constant at higher frequencies ε_∞ , the thicknesses determined from the fitting, and the figure of merit (FOM) of the fittings. The estimated thicknesses are in agreement with those obtained from profilometry and SEM providing support to the theoretical models used to simulate the spectra.

Figure 10 shows the dispersion of the refractive index n and the extinction coefficient k of the crystalline films. Figure 10a compares the films presenting the same fluorite-type structure: BO, BNO-20, BNO-30, and BNO-50. The

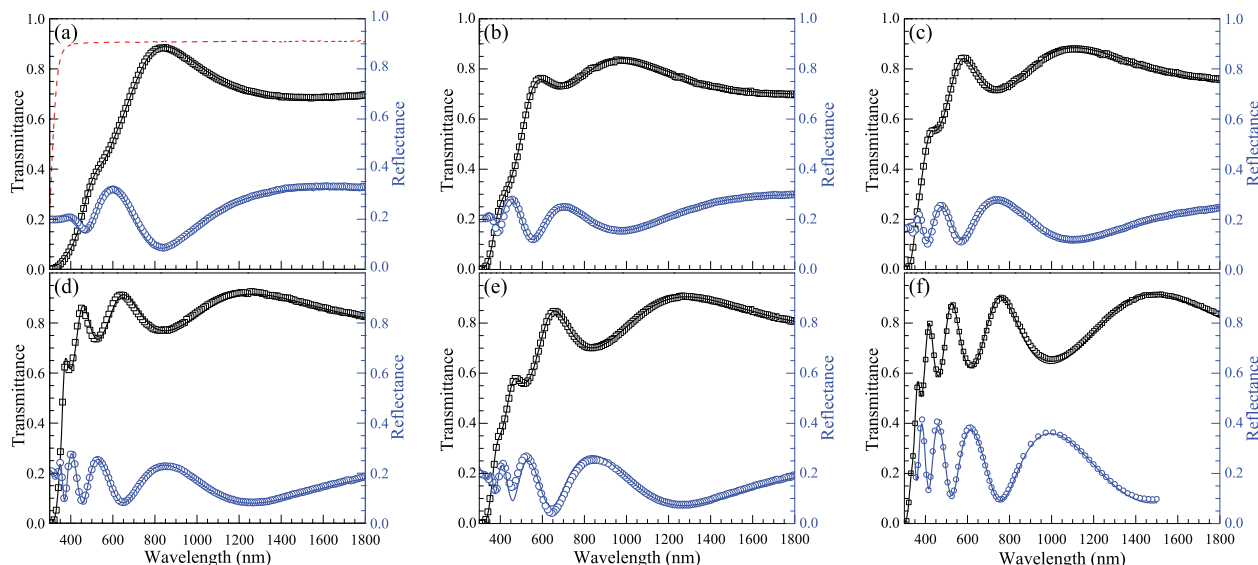


Figure 9. Experimental and fitted spectra of transmittance (T) and reflectance (R) measured corresponding to a) BO, b) BNO-20, c) BNO-30, d) BNO-50, e) BNO-70-TT, f) BNO-100-TT films. Squares and circles represent the experimental T and R data, respectively; the solid lines represent the fitted data; and the dashed line in a) represents the T spectrum of the Corning[®] 7059 glass.

refractive index tends to decrease as the power applied to the Nb target increases, effect that might be associated to variations in the film density (see Table 1) when the Nb replace Bi ions in the structure. It can also be observed that the extinction coefficient, k , becomes nonzero at higher energies as the Nb content increases, indicating that the optical absorption lowers as Nb content increases and suggesting that solid solutions with more Nb concentration have higher optical gaps. The complex dielectric functions are shown in Figure S5 of the Supporting Information.

Figure 10b shows the n and k spectra of the Nb-rich samples: $\text{Bi}_5\text{Nb}_3\text{O}_{15}$ phase (BNO-70-TT sample), and the mixture of BiNbO_4 polymorphs (BNO-100-TT sample). These films have different crystalline structures respect to the fluorite-structure samples, that is, their electronic structures are dissimilar which

might affect the polarizability and the related refractive index; therefore, the differences observed between the n spectra cannot be explained considering only the mass density.

A comparison of the refractive index for all samples at 2.25 eV (equivalent to 550 nm) is shown in Table 3. The refractive indexes of all samples are higher than 2 in the middle of the visible range (550 nm or 2.25 eV). This is common in metallic oxides, and the high value of n suggests the use of the BNOs in optical applications such as: wave guides, antireflection films, holographic materials, photonic crystals, LEDs, and so on, especially the films with high transparency in the visible range.^[52]

In the literature, the dispersion of the refractive index, $n(E)$, has been reported only for II- Bi_3NbO_7 , α -, and β - BiNbO_4 phases. Kang et al.^[51] calculated the n and k spectra of a crystalline Bi_3NbO_7 film from the data measured by spectroscopic

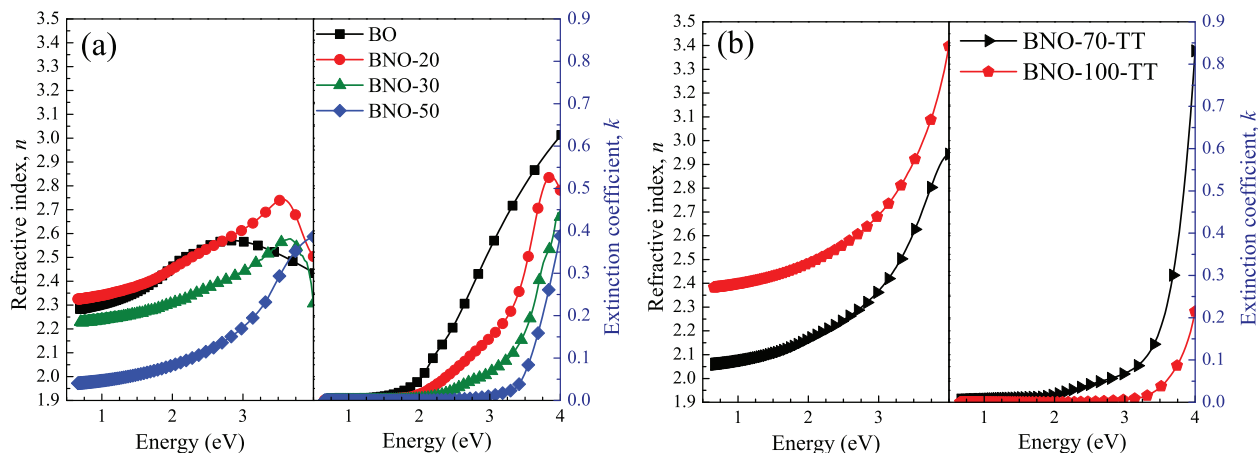


Figure 10. Optical properties: refractive index and extinction coefficient spectra determined by UV-Visible-NIR T&R spectrometry corresponding to a) the phases with fluorite-type structure and b) the films with $\text{Bi}_5\text{Nb}_3\text{O}_{15}$ and the mixture of BiNbO_4 polymorphs.

Table 3. Refractive index n at 2.25 eV and the optical gap (E_g) values estimated by the fitting of parametric models to the experimental data measured by UV-Visible-NIR spectrometry.

Sample	Identified phases	Refractive index n , at 2.25 eV	Optical gap, E_g [eV]	Reported optical gaps [eV]
BO	δ -Bi ₂ O ₃	2.51	1.67	1.5 ^[35] ; 1.73–1.95 ^[44]
BNO-20	S.S. 5.1 at% Nb	2.50	2.81	
BNO-30	S.S. 6.6 at% Nb	2.34	2.92	
BNO-50	II-Bi ₃ NbO ₇	2.07	3.22	2.43 ^[7a] ; 2.72 ^[55] ; 3.07 ^[51,a]
BNO-70-TT	Bi ₅ Nb ₃ O ₁₅	2.20	3.25	2.90 ^[7d] ; 3.25 ^[7c]
BNO-100-TT	BiNbO ₄ (76 wt% α + 24 wt% β)	2.52	3.34	α : 2.8 ^[7e] ; 3.2 ^[56] ; 3.73 ^[53] β : 2.78 ^[7g] ; 3.05 ^[57] ; 3.2 ^[51,a] ; 3.15 ^[53] ; 2.64–3.69 ^[58] $\alpha + \beta$: 2.93 ^[7f] ; 2.88–2.91 ^[7g]

^{a)} Optical gaps of BNOs as thin films.

ellipsometry. The refractive index values are higher than those reported in this work. However, this discrepancy is probably related to the characterization technique, since the ellipsometric analysis of our BNO films deposited on Si also shows refractive indexes slightly larger than those obtained by the T&R measurements, while the extinction coefficients were independent of the technique (see Figure S6 of the Supporting Information).

Nevertheless, there is a good resemblance in the n and k spectral shapes between Kang et al.^[51] and our solid solutions spectra. Kang et al.^[51] reported a maximum corresponding to an interband transition around 3.7 eV, similar to the n spectra of the BNO-20 and BNO-30 films. Although in the BNO-50 spectrum, a maximum is not observed, the fitted parameters (Table S1) show that the first oscillator has a resonance energy (E_0) at 3.8 eV, but its amplitude is very low, and for this reason it cannot be distinguished.

Similarly, the n spectrum corresponding to β -BiNbO₄ reported by Kang et al.^[51] is very similar to the spectrum of the BNO-100-TT film, despite that our film has a mixture of polymorphs. In addition, the shape of the $n(E)$ curve for the BNO-100-TT film is very similar to the theoretically calculated dispersion for the α - and β -BiNbO₄ phases done by Litimein et al.,^[53] which clearly show that both polymorphs have nearly identical dispersion curves, making difficult their identification based on their optical properties.

The optical band gap was estimated from the absorption coefficient, α , dispersion curve, assuming indirect transition bands for all samples. **Figure 11** shows an example of the calculation of the optical gap using the plot for indirect transitions. The fundamental transition was assumed as indirect band, because the gap estimations supposing direct band transitions led to unrealistic high energy gaps in contradiction with the energy values where the transmittance drop begins. Moreover, it is very common that nanocrystalline films (see Table 1) with a large fraction of grain boundaries are better represented by indirect or Tauc-type optical band gaps. Furthermore, this is the reason to use the Tauc–Lorentz model for the fittings, since it has been demonstrated that the model is valid for nanocrystalline materials.^[54]

The optical gap values are summarized in Table 3, adding also the reported gaps estimated from diffuse reflectance

measurements of BNOs powders or theoretical calculations. The E_g values increase from 1.67 to 3.34 eV, as the Nb content increases from 0 to 16.1 at%. The reported optical gaps of both components of the pseudo-binary system are Bi₂O₃ (δ -phase: 1.5 eV)^[35] and Nb₂O₅ (3.4 eV),^[33] thus it was expected that the optical gaps of the evaluated films in this work are within this range.

The optical gaps of the Bi₃NbO₇, Bi₅Nb₃O₁₅ y BiNbO₄ phases have been previously reported, while those of solid solutions with type II structure have not. Comparison with the reported values (see Table 3) indicates that the E_g values calculated in this work are close to the reported optical gaps of BNOs films and the theoretically calculated ones, but lower than the estimated gaps using BNOs powder samples, in almost all of the cases. According to our experience^[27] it is expected that films have lower optical gaps than the powders, because the nanocrystalline films have a high density of defects originated mainly by the large density of crystal boundaries, hence band tails or absorption at lower energies are generated.

The E_g values of the different deposited BNOs films show that the films with Nb content below 9.2 at% are semiconductors with

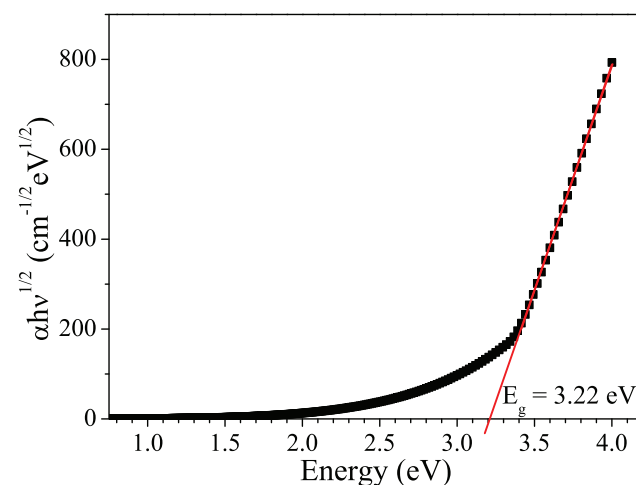


Figure 11. Example of the optical gap calculation assuming indirect fundamental transition.

band gaps into the visible light range; at this Nb concentration and above it the phases are wide band gap semiconductors, that is, with gaps in the UV range. Consequently, the inclusion of these BNO films in devices for photo-activated processes would need different irradiation energies (visible or UV light) depending of the Nb content.

Summarizing, the results of this work have demonstrated that by using a plasma-assisted technique it was possible to synthesize complex compounds. The term “synthesis” of BNOs is used along the text because the experiments did not rely on the transference of the composition from a single target to the substrates, instead the ternary oxides were formed starting from the sputtering of two different and independently driven targets with the elements of the $\text{Bi}_2\text{O}_3\text{--Nb}_2\text{O}_5$ system.

Some compounds were obtained at relatively lower substrate or annealing temperatures in comparison to the previous works related to the deposition of BNOs films by PVD^[8e,f,15,16] or chemical methods.^[8i] This finding could be an advantage for applications such as the fabrication of microelectronic circuits on polymeric substrates.

4. Conclusions

The dual co-sputtering technique, starting from two independently driven targets Bi_2O_3 and Nb, allows the successful synthesis of a wide range of phases belonging to the $\text{Bi}_2\text{O}_3\text{--Nb}_2\text{O}_5$ system with a precise control on the composition by the variation of the power applied to the metallic target. This fact leads to the use of plasma-assisted deposition technique as an alternative method to synthesize ternary, or more complex, oxides at nanometric dimensions for the fabrication of high-tech devices. As-deposited crystalline films were obtained when the Nb content was lower or equal to 9.2 at% (50 W applied to the Nb target). However, for larger Nb contents, the films were amorphous even when the deposition temperature was increased. Nevertheless, when the amorphous films were annealed at 600 °C, it was possible to obtain a crystalline phase of the corresponding BNO compound: $\text{Bi}_5\text{Nb}_3\text{O}_{15}$ for Nb content of 12.5 at% and finally, BiNbO_4 for 16.1 at%. The crystalline phases obtained using co-sputtering and post-annealing were: $\delta\text{-Bi}_2\text{O}_3$ (as reference phase without Nb), solid solutions with type II (based on defective fluorite-type structure) structure and Nb concentrations of: 5.1 and 6.6 at%; II- Bi_3NbO_7 , $\text{Bi}_5\text{Nb}_3\text{O}_{15}$, and a mixture of 76 wt% of $\alpha\text{-BiNbO}_4$ + 24 wt% of $\beta\text{-BiNbO}_4$.

The energy dependence of the refractive index and the extinction coefficient, as well as the optical gap of the BNO films were determined from the fitting of parametric models applied to the experimental transmittance and reflectance measured by UV-Visible-NIR spectrometry. The optical properties indicate that the films could be possible candidate materials for applications associated with optical devices thanks to their high refractive index n (2–3) in the visible range, and with photo-activated processes under visible irradiation in the case of the solid solutions with 5.1 and 6.6 at% of Nb ($E_g = 2.81, 2.92$ eV, respectively) or UV irradiation in the case of II- Bi_3NbO_7 , $\text{Bi}_5\text{Nb}_3\text{O}_{15}$, and BiNbO_4 niobates ($E_g = 3.22, 3.25, 3.34$ eV, respectively).

Supporting Information

Supporting Information is available from the Wiley Online Library or from the author.

Acknowledgements

The research leading to these results has received funding from the European Community Seven Framework Program and CONACYT (BisNano project No 263878 and 125141), PHOCSCLEEN (FP7-318977), and CONACYT (251279). O.D-R. thanks to CONACYT and DGAPA-CIC-UNAM for the doctoral and postdoctoral fellowships. Also, the authors thank the support of the academic technicians Adriana Tejeda, Omar Novelo, Josué Romero, Lazaro Huerta, Hermilo Zarco, and Anna Cantaluppi-Harlé. (Supporting Information is available online from Wiley InterScience or from the author).

Conflict of Interest

The authors declare no conflict of interest.

Keywords

bismuth niobates, dual co-sputtering, optical gap, optical properties, oxide materials, thin films

Received: March 18, 2017

Revised: June 4, 2018

Published online: July 4, 2018

- [1] A. Di Paola, E. Garcia-Lopez, G. Marci, L. Palmisano, *J. Hazard. Mater.* **2012**, *211*, 3.
- [2] M. Čebela, D. Zagorac, K. Batalović, J. Radaković, B. Stojadinović, V. Spasojević, R. Hercigonja, *Ceram. Int.* **2017**, *43*, 1256.
- [3] R. Mohan, *Nat. Chem.* **2010**, *2*, 336.
- [4] a) S. Sanna, V. Esposito, J. W. Andreasen, J. Hjelm, W. Zhang, T. Kasama, S. B. Simonsen, M. Christensen, S. Linderoth, N. Pryds, *Nat. Mater.* **2015**, *14*, 500; b) J. Sottmann, M. Herrmann, P. Vajeeston, A. Ruud, C. Drathen, H. Emerich, D. S. Wragg, H. Fjellvåg, *Chem. Mater.* **2017**, *29*, 2803.
- [5] a) M. Mehring, *Coordin. Chem. Rev.* **2007**, *251*, 974; b) L. Chen, W. Guo, Y. X. Yang, A. Zhang, S. Q. Zhang, Y. H. Guo, Y. N. Guo, *Phys. Chem. Chem. Phys.* **2013**, *15*, 8342; c) X. Liu, M. Zhou, G. Yao, W. Shi, C. Ma, P. Lv, Y. Tang, Y. Yan, *RSC Adv.* **2014**, *4*, 18264.
- [6] a) T. Takahashi, H. Iwahara, *Mater. Res. Bull.* **1978**, *13*, 1447; b) A. V. Joshi, S. Kulkarni, J. Nachlas, J. Diamond, N. Weber, A. V. Virkar, *J. Mater. Sci.* **1990**, *25*, 1237; c) A. A. Yaremchenko, V. V. Kharton, E. N. Naumovich, A. A. Vecher, *J. Solid State Electrochem.* **1998**, *2*, 146; d) X. P. Wang, G. Corbel, S. Kodjikian, Q. F. Fang, P. Lacorre, *J. Solid State Chem.* **2006**, *179*, 3338; e) C. D. Ling, S. Schmid, P. E. R. Blanchard, V. Petricek, G. J. McIntyre, N. Sharma, A. Maljuk, A. A. Yaremchenko, V. V. Kharton, M. Gutmann, R. L. Withers, *J. Am. Chem. Soc.* **2013**, *135*, 6477.
- [7] a) G. K. Zhang, J. L. Yang, S. M. Zhang, Q. Xiong, B. B. Huang, J. T. Wang, W. Q. Gong, *J. Hazard. Mater.* **2009**, *172*, 986; b) Q. Wang, L. Yuan, M. Dun, X. Yang, H. Chen, J. Li, J. Hu, *Appl. Catal., B* **2016**, *196*, 127; c) K. Gurunathan, P. Maruthamuthu, *J. Solid State Electrochem.* **1998**, *2*, 176; d) S. Q. Zhang, Y. X. Yang, Y. N. Guo, W. Guo, M. Wang, Y. H. Guo, M. X. Huo, *J. Hazard. Mater.* **2013**, *261*, 235; e) S. S. Dunkle, K. S. Suslick, *J. Phys. Chem. C* **2009**, *113*, 10341;

- f) R. Ullah, H. M. Ang, M. O. Tade, S. B. Wa *Chem. Eng. J.* **2012**, *185*, 328; g) H. Zhai, S. Shang, L. Zheng, P. Li, H. Li, H. Luo, J. Kong, *Nanoscale Res. Lett.* **2016**, *11*, 383.
- [8] a) M. Valant, D. Suvorov, *J. Am. Ceram. Soc.* **2003**, *86*, 939; b) P. Samoukhina, S. Kamba, S. Santhi, J. Petzelt, M. Valant, D. Suvorov, *J. Eur. Ceram. Soc.* **2005**, *25*, 3085; c) T. Takenaka, K. Komura, K. Sakata, *Jpn. J. Appl. Phys.* **1996**, *35*, 5080; d) A. Lisinska-Czekaj, D. Czekaj, *Key Eng. Mater.* **2012**, *512–515*, 1212; e) J.-H. Park, S.-G. Yoon, H.-D. Kang, J.-W. Lee, W.-C. Kim, S.-T. Lim, S.-H. Sohn, J.-S. Moon, H.-J. Jin, H.-M. Jung, S.-E. Lee, Y.-K. Chung, *J. Electrochem. Soc.* **2006**, *153*, F225; f) K.-H. Cho, C.-H. Choi, Y. H. Jeong, S. Nahm, C.-Y. Kang, S.-J. Yoon, H.-J. Lee, *J. Electrochem. Soc.* **2008**, *155*, G148; g) H.-W. Lee, W.-J. Lee, S.-G. Yoon, *Electrochem. Solid-State Lett.* **2009**, *12*, G23; h) T. Ariga, S. Inoue, S. Matsumoto, M. Onoue, T. Miyasako, E. Tokumitsu, T. Shimoda, *Jpn. J. Appl. Phys.* **2015**, *54*, 091501; i) L. F. Goncalves, L. S. R. Rocha, C. C. Silva, J. A. Cortés, M. A. Ramirez, A. Z. Simões, *J. Mater. Sci.: Mater. Electron.* **2016**, *27*, 2866.
- [9] R. S. Roth, J. L. Waring, *J. Res. Natl. Bur. Stand., Sect. A* **1962**, *66*, 451.
- [10] W. Zhou, D. A. Jefferson, J. M. Thomas, *Proc. R. Soc. London, Ser. A* **1986**, *406*, 173.
- [11] A. Castro, E. Aguado, J. M. Rojo, P. Herrero, R. Enjalbert, J. Galy, *Mater. Res. Bull.* **1998**, *33*, 31.
- [12] S. Tahara, A. Shimada, N. Kumada, Y. Sugahara, *J. Solid State Chem.* **2007**, *180*, 2517.
- [13] a) N. V. Chezhina, D. A. Korolev, A. V. Fedorova, N. A. Zhuk, V. A. Butin, V. P. Lutoev, B. A. Makeev, S. S. Shevchuk, A. N. Nizovtsev, *Russ. J. Gen. Chem.* **2017**, *87*, 899; b) N. A. Zhuk, I. V. Piir, A. L. Pimenov, N. V. Chezhina, **2008**, *78*, 335.
- [14] S.-Y. Jeon, N.-J. Seong, J.-K. Ahn, H.-W. Lee, S.-G. Yoon, *Nanotechnol.* **2008**, *19*, 435305.
- [15] S. Chattopadhyay, P. Ayyub, R. Pinto, M. S. Multani, *J. Mater. Res.* **1998**, *13*, 1113.
- [16] T. G. Seong, K. H. Cho, J. Y. Choi, S. Nahm, C. Y. Kang, S. J. Yoon, J. H. Kim, *J. Phys. D: Appl. Phys.* **2009**, *42*, 175402.
- [17] G. Szwachta, S. Kaç, T. Moskalewicz, *Surf. Coat. Technol.* **2016**, *302*, 474.
- [18] K. Nishimura, T. Yabumoto, A. Yuasa, N. Fujita, H. Ito, N. Miura, S. Matsumoto, H. Matsumoto, *J. Vac. Soc. Jpn.* **2011**, *54*, 325.
- [19] a) N. R. Murphy, C. V. Ramana, L. Sun, J. G. Jones, J. T. Grant, *J. Alloys Compd.* **2017**, *708*, 947; b) A. S. Yusof, Z. Hassan, N. Zainal, *Mater. Res. Bull.* **2018**, *97*, 314; c) S.-J. Shen, T.-S. Yang, M.-S. Wong, *Surf. Coat. Technol.* **2016**, *303*, 184.
- [20] D.-H. Kim, E. Byon, G.-H. Lee, S. Cho, *Thin Solid Films* **2006**, *510*, 148.
- [21] R. Mirabal-Rojas, O. Depablos-Rivera, S. M. Thalluri, J. C. Medina, M. Bizarro, J. Perez-Alvarez, S. E. Rodil, A. Zeinert, *Appl. Phys. A* **2016**, *122*, 325.
- [22] T. Tanaka, T. Nagatomo, D. Kawasaki, M. Nishio, Q. Guo, A. Wakahara, A. Yoshida, H. Ogawa, *J. Phys. Chem. Solids* **2005**, *66*, 1978.
- [23] a) M. Kumar, R. Mitra, *Surf. Coat. Technol.* **2014**, *251*, 239; b) H. Bakkali, E. Blanco, M. Dominguez, M. B. de la Mora, C. Sánchez-Aké, M. Villagrán-Muniz, *Appl. Surf. Sci.* **2017**, *405*, 240.
- [24] a) B. Cantor, R. W. Cahn, *Acta Metall.* **1976**, *24*, 845; b) A. Bahrami, J. P. Álvarez, O. Depablos-Rivera, R. Mirabal-Rojas, A. Ruíz-Ramírez, S. Muhl, S. E. Rodil, **2018**, *20*, 1700687.
- [25] H. Shang, F. Ding, G. Li, L. Wang, F. Qu, H. Zhang, Z. Dong, H. Zhang, Z. Gao, W. Zhou, H. Gu, *J. Alloys Compd.* **2017**, *726*, 532.
- [26] a) K. Cheng, Y. Huang, J. Liu, M. Xue, Z. Kuang, Z. Lu, S. Wu, Z. Du, *J. Alloys Compd.* **2016**, *684*, 237; b) G. P. Bernhardt, J. I. Krassikoff, B. T. Sturtevant, R. J. Lad, *Surf. Coat. Technol.* **2014**, *258*, 1191; c) M. Mazur, J. Domaradzki, D. Wojcieszak, D. Kaczmarek, *Surf. Coat. Technol.* **2018**, *334*, 150.
- [27] O. Depablos-Rivera, J. C. Medina, M. Bizarro, A. Martínez, A. Zeinert, S. E. Rodil, *J. Alloys Compd.* **2017**, *695*, 3704.
- [28] R. W. Cheary, A. Coelho, *J. Appl. Crystallogr.* **1992**, *25*, 109.
- [29] N. C. Halder, C. N. J. Wagner, *Acta Crystallogr.* **1966**, *20*, 321.
- [30] D. A. G. Bruggeman, *Ann. Phys. Berlin* **1935**, *24*, 636.
- [31] G. E. Jellison, F. A. Modine, *Appl. Phys. Lett.* **1996**, *69*, 371.
- [32] C. C. Kim, J. W. Garland, H. Abad, P. M. Raccah, *Phys. Rev. B* **1992**, *45*, 11749.
- [33] C. Nico, T. Monteiro, M. P. F. Graça, *Prog. Mater. Sci.* **2016**, *80*, 1.
- [34] R. Mirabal-Rojas, S. Muhl, S. E. Rodil, E. Camps, M. Lejeune, A. Zeinert, *J. Vac. Sci. Technol. A* **2016**, *34*, 041518.
- [35] C. L. Gomez, O. Depablos-Rivera, P. Silva-Bermudez, S. Muhl, A. Zeinert, M. Lejeune, S. Charvet, P. Barroy, E. Camps, S. E. Rodil, *Thin Solid Films* **2015**, *578*, 103.
- [36] A. V. Naumkin, A. Kraut-Vass, S. W. Gaarenstroom, C. J. Powell, NIST X-ray Photoelectron Spectroscopy Database, Version 4.1, National Institute of Standards and Technology, Gaithersburg **2012**. <http://srdata.nist.gov/xps/>.
- [37] C. L. Gomez, O. Depablos-Rivera, J. C. Medina, P. Silva-Bermudez, S. Muhl, A. Zeinert, S. E. Rodil, *Solid State Ionics* **2014**, *255*, 147.
- [38] C. Morant, J. M. Sanz, L. Galán, *Phys. Rev. B* **1992**, *45*, 1391.
- [39] G. Silversmit, D. Depla, H. Poelman, G. B. Marin, R. De Gryse, *Surf. Sci.* **2006**, *600*, 3512.
- [40] S. Inoue, T. Ariga, S. Matsumoto, M. Onoue, T. Miyasako, E. Tokumitsu, N. Chinone, Y. Cho, T. Shimoda, *J. Appl. Phys.* **2014**, *116*, 154103.
- [41] a) H. F. Zhai, X. Qian, J. Z. Kong, A. D. Li, Y. P. Gong, H. Li, D. Wu, *J. Alloys Compd.* **2011**, *509*, 10230; b) B. Muktha, J. Darriet, G. Madras, T. N. G. Row, *J. Solid State Chem.* **2006**, *179*, 3919.
- [42] N. Wang, M. Y. Zhao, Z. W. Yin, W. Li, *Mater. Lett.* **2003**, *57*, 4009.
- [43] M. Onoue, T. Miyasako, E. Tokumitsu, T. Shimoda, *IEICE Electronics Express* **2014**, *11*, 20140651.
- [44] H. T. Fan, X. M. Teng, S. S. Pan, C. Ye, G. H. Li, L. D. Zhang, *Appl. Phys. Lett.* **2005**, *87*, 231916.
- [45] L. V. Ermakova, V. N. Strekalovskii, E. G. Vovkotrub, V. G. Bamburov, *J. Appl. Spectrosc.* **2002**, *69*, 152.
- [46] H. T. Fan, S. S. Pan, X. M. Teng, C. Ye, G. H. Li, *J. Phys. D Appl. Phys.* **2006**, *39*, 1939.
- [47] P. Ayyub, M. S. Multani, V. R. Palkar, R. Vijayaraghavan, *Phys. Rev. B* **1986**, *34*, 8137.
- [48] K. Chang, D. Music, M. to Baben, D. Lange, H. Bolvardi, J. M. Schneider, *Sci. Technol. Adv. Mater.* **2016**, *17*, 210.
- [49] a) N. M. Sammes, G. A. Tompsett, H. Nafe, F. Aldinger, *J. Eur. Ceram. Soc.* **1999**, *19*, 1801; b) A. M. Azad, S. Larose, S. A. Akbar, *J. Mater. Sci.* **1994**, *29*, 4135.
- [50] C. L. Gomez, S. E. Rodil, *Solid State Ionics* **2017**, *309*, 100.
- [51] Y. J. Kang, T. H. Ghong, Y. W. Jung, J. S. Byun, S. Kim, Y. D. Kim, T. G. Seong, K. H. Cho, S. Nahm, *Thin Solid Films* **2010**, *518*, 6526.
- [52] Y. Cheng, C. Lü, B. Yang, *Recent Pat. Mater. Sci.* **2011**, *4*, 15.
- [53] F. Litimein, R. Khenata, S. K. Gupta, G. Murtaza, A. H. Reshak, A. Bouhemadou, S. Bin Omran, M. Yousaf, P. K. Jha, *J. Mater. Sci.* **2014**, *49*, 7809.
- [54] A. E. Naciri, F. Ahmed, M. Stchakovsky, *Thin Solid Films* **2011**, *519*, 2843.
- [55] L. Wang, W. Z. Wang, M. Shang, S. M. Sun, W. Z. Yin, J. Ren, J. Zhou, *J. Mater. Chem.* **2010**, *20*, 8405.
- [56] C. Balamurugan, D. W. Lee, A. R. Maheswari, M. Parmar, *RSC Adv.* **2014**, *4*, 54625.
- [57] R. Yu, A. Fan, M. Yuan, T. Li, J. Wang, *Phys. Chem. Chem. Phys.* **2016**, *18*, 23702.
- [58] K. Ding, B. Chen, Y. Li, Y. Zhang, Z. Chen, *J. Mater. Chem. A* **2014**, *2*, 8294.